Chem

CellPress

Article

Interfacial and Nanoconfinement Effects Decrease the Excited-State Acidity of Polymer-Bound Photoacids

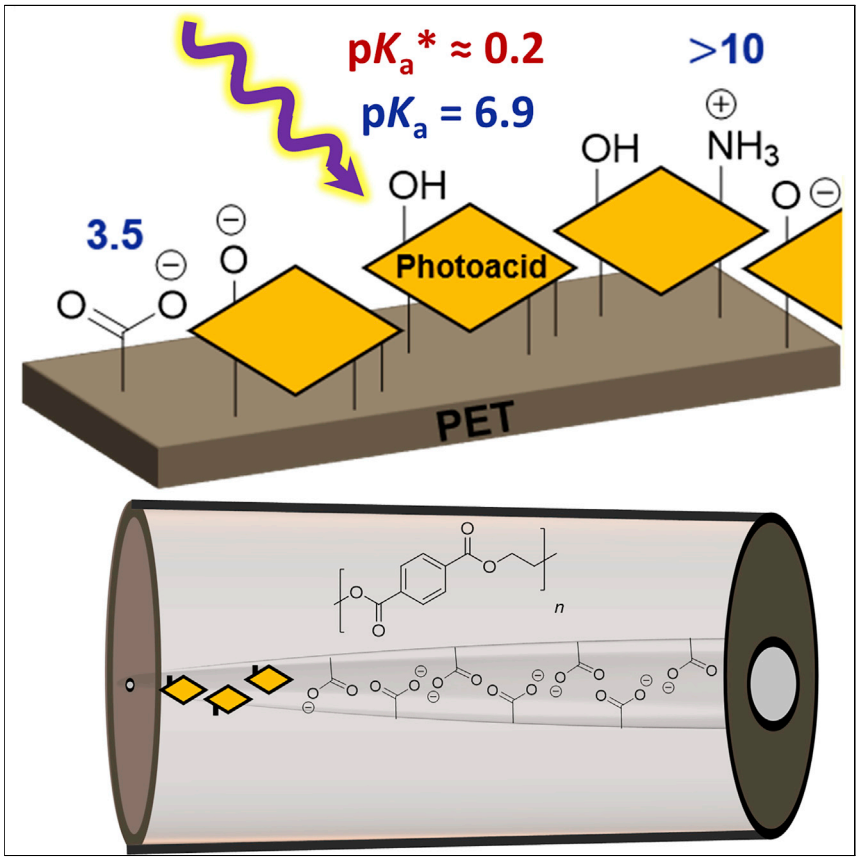

We previously reported photovoltaic action from photoacid-dye-modified ion-exchange membranes. A more controlled model system for those materials are photoacid-modified nanopores in poly(ethylene terephthalate) reported herein. Photoacids bound to the sub-10-nm-sized tips of these nanoporous poly(ethylene terephthalate) materials exhibited decreases in ground-state and excited-state acidity versus the same photoacid dyes dissolved in solution. The data indicate that nano-confinement and local electrostatics are important considerations when designing light-to-ionic energy conversion devices with possible applications in energy conversion and neuron triggering.

Christopher D. Sanborn, Jenu Varghese Chacko, Michelle Digman, Shane Ardo

ardo@uci.edu

HIGHLIGHTS

Binding photoacids to conical nanopores decreases their acidity

When photoacids are bound to nanopores they exhibit less excited-state proton transfer

The acidity and density of functional groups in single nanopores is quantified

Sanborn et al., Chem 5, 1648–1670
June 13, 2019
https://doi.org/10.1016/j.chempr.2019.04.022

Chem

CellPress

Article

Interfacial and Nanoconfinement Effects Decrease the Excited-State Acidity of Polymer-Bound Photoacids

Christopher D. Sanborn,[1] Jenu Varghese Chacko,[2] Michelle Digman,[2] and Shane Ardo[1,3,4,5,*]

SUMMARY

Photo-initiated ion transport on the nanoscale is relevant to various fields including energy conversion, neuron triggering, and biomimetic processes. To study this phenomenon, we synthesized and evaluated photoacid-modified polymers, which generate hydrated protons in response to visible-light excitation. Pyrenol photoacid dye molecules were covalently bonded within conical nanopores that had been track etched in poly(ethylene terephthalate). The data suggest that ~90% of the nanopore surfaces were modified with photoacids and that photoacids were, on average, bound through three sulfonamide groups. In comparison to photoacids dissolved in an aqueous solution, photoacids bound specifically to the nanoporous tip region were, on average, weaker acids in their ground and excited states, which we presume is due to differences in surface potential or solvation environment in the confined nanopores. These results suggest that ion transport initiated by nanoconfined photoacids will require careful molecular engineering to enable efficient light-to-ionic energy conversion.

INTRODUCTION

Control of the direction and timing of energy and charge transport on the nanoscale and macroscale has allowed for various innovations, from advanced microelectronics and photovoltaics to life. While in most artificial systems energy and charge are transported using electronic processes,[1] nature on the other hand also uses ionic processes.[2,3] For example, action potentials are transmitted along neurons via a series of orchestrated ion fluxes across lipid bilayers,[4] and the photosynthetic processes in photosystem II of green plants involve orthogonal transport of electrons and protons.[5] In each of these biological systems, an asymmetry across the membrane leads to a preferential direction for species transport often based on the sign of their charge[6–9] and which is manifest as current rectification.

Several artificial systems have also been shown to rectify ionic current: ion-exchange membranes,[10–14] nanopores,[15–26] and nanopipettes.[27–32] Utilizing the materials asymmetry that results in this current rectification, light-driven proton pumps have been demonstrated.[33–36] However, until recently,[37–39] none of these materials utilized covalently bound photoacid-dye molecules.[40,41] Photoacids enable direct conversion of light energy into a change in electrochemical potential of protons and are therefore well-suited for light-driven proton pumping. Photon absorption by a photoacid dye results in a decrease in the pK_a of one of its protic functional groups, therefore making it more acidic in its excited state.[42] This results in net

The Bigger Picture

A major challenge facing humanity is the availability of clean and potable water for human consumption and agriculture. Over time, this problem is expected to worsen because of population growth and increases in the severity and frequency of global climate disruption. As such, new technologies for low-cost, efficient, and distributed desalination of salt water are desired. Toward this, our group recently reported ion-selective membranes that directly pump ions when illuminated with sunlight. A critical component in the technology is the polymer-bound photoacid dye, which is carefully characterized herein. In our initial materials systems, controlled quantitative measurements of the properties of polymer-bound photoacids were extremely challenging. Using the knowledge gained from studies herein, we are hopeful that the efficiency of our technology can be increased rapidly, to a point where it enables inexpensive and autonomous desalination of distributed saltwater sources.

liberation of a proton charge carrier that can then be transported in a direction that is dictated by the electrostatic asymmetry of the material to which it is bound. If the built-in asymmetry of the material results in ionic current rectification due to the presence of selective contacts on each side of the material,[43] light should impart vectorial pumping of ions. Recently, we demonstrated that photoacid-dye-modified Nafion ion-exchange membranes exhibit photovoltaic action when illuminated with visible light.[37,39] Absorption of light by Nafion-bound photoacids resulted in a change in the local concentration of protons,[44,45] thus perturbing the chemical speciation within the hydrated charged nanopores of Nafion away from its initial state and generating a small photovoltage. The observation of a photocurrent was consistent with directional ion transport of the photo-liberated protons driven by an asymmetry in the hydrated charged nanopores of Nafion. The mechanistic causes for this small photovoltage and small photocurrent from unoptimized photoacid-dye-modified Nafion are not well understood. This prompted us to further study the fundamental photophysical properties of photoacid-dye molecules bound to hydrated charged nanoporous polymers, such as Nafion and poly(ethylene terephthalate) (PET).

Herein, we utilize charged polymer nanopores as model systems for ion-exchange membranes to further interrogate the photovoltaic ion-pumping process previously observed in photoacid-dye-modified Nafion. Nanopores are excellent models for ion-exchange membranes, like Nafion, because Nafion phase segregates into micelle-like hydrophilic regions that are spaced on the order of several nanometers and bear negatively charge covalently bound (fixed) sulfonate groups on their interior.[46–48] The model systems that we utilize herein consist of ion-rectifying track-etched conical nanopores in PET with tip diameters as small as several nanometers and bearing negatively charged fixed carboxylate groups on their interior. Through careful characterization of these model nanoporous rectifying materials functionalized with custom photoacid molecules, we further elucidated the role that confinement plays on the photophysical properties of the bound photoacid-dye molecules. Our results may help explain some of the limitations in the light-driven ion pumping process that we observed using photoacid-dye-modified Nafion membranes.

RESULTS AND DISCUSSION

Molecular Synthesis of a Bondable Photoacid Molecule

Custom photoacid, tris(sulfonamide)pyrenol **1**, was synthesized from pyranine using a four-step synthetic protocol (Scheme 1). Pyranine was treated with acetic anhydride under alkaline conditions to afford an acetyl-protected hydroxyl group followed by refluxing in excess thionyl chloride with catalytic *N,N*-dimethylformamide to activate the three sulfonate groups as sulfonyl chlorides. In a solution of 2:7:1 THF:CH_3CN:H_2O (v/v/v), two equivalents of *N*-Boc-ethylenediamine per sulfonyl chloride were added such that one equivalent formed the sulfonamide and HCl, which was neutralized by the other equivalent. The product was then deacetylated via addition of NaOH, and the Boc protecting group was removed via trifluoroacetic acid treatment to yield **1**. Additional purification was achieved using reverse-phase high-performance liquid chromatography.

Measurement of Acid Dissociation Constants for Photoacids in Solution

The most acidic pK_a value of **1** dissolved in aqueous buffered solution was determined to be 5.80 $\pm$ 0.03 via an acid–base titration procedure with spectrophotometric detection and non-linear least-squares fitting of the data to the Hill equation

[1]Department of Chemistry, University of California, Irvine, Irvine, CA 92697, USA

[2]Department of Biomedical Engineering, University of California, Irvine, Irvine, CA 92697, USA

[3]Department of Materials Science & Engineering, University of California, Irvine, Irvine, CA 92697, USA

[4]Department of Chemical & Biomolecular Engineering, University of California, Irvine, Irvine, CA 92697, USA

[5]Lead Contact

*Correspondence: ardo@uci.edu

https://doi.org/10.1016/j.chempr.2019.04.022

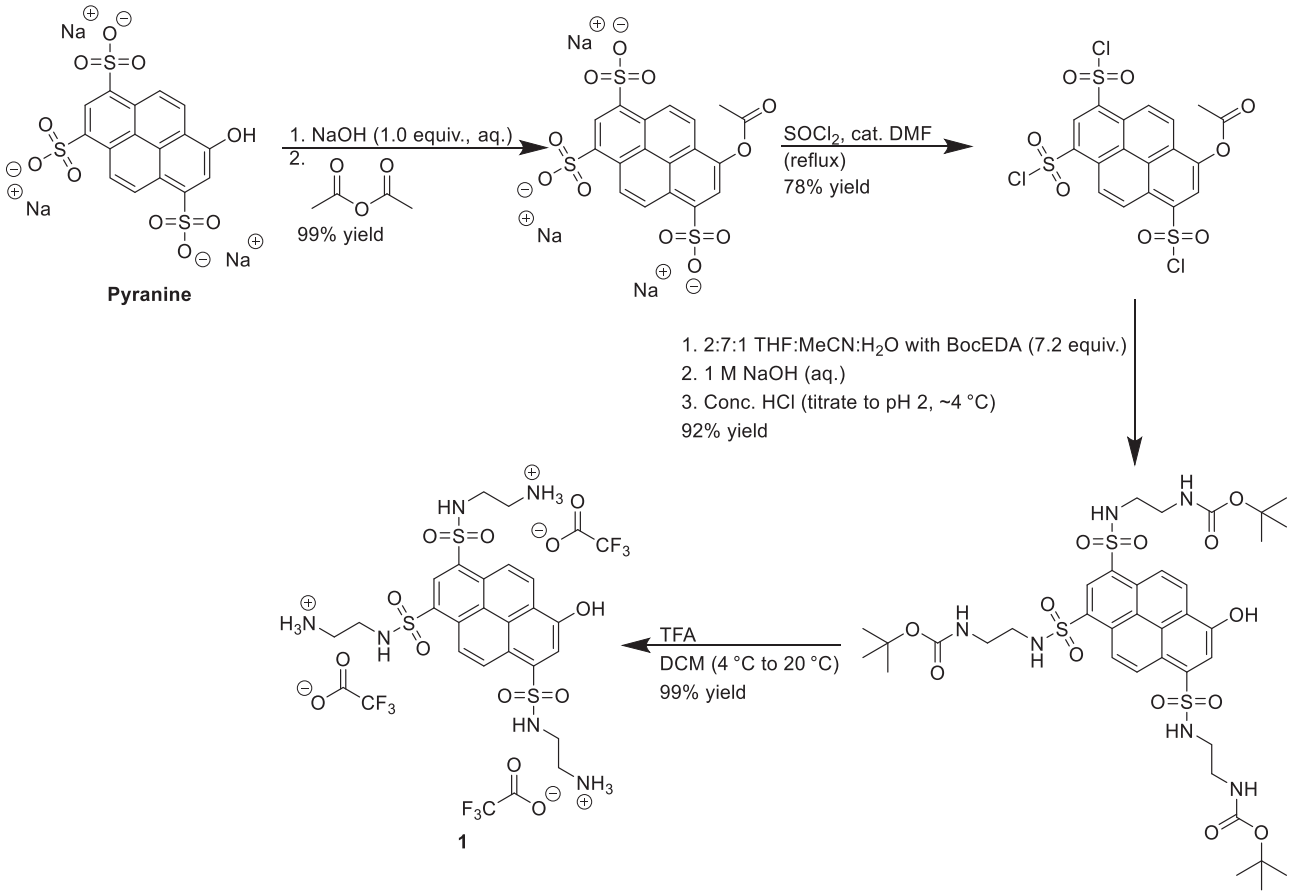

Scheme 1. Photoacid Synthetic Protocol

Synthesis of **1** from pyranine by sulfonate activation.
See also Figures S14 and S15.

(Figures 1A and 1B; see Supplemental Experimental Procedures, Determination of pK_a Values):

$$\theta = \frac{1}{1 + 10^{\,n(\mathrm{pH}-\mathrm{p}K_a)}}, \qquad \text{(Equation 1)}$$

where θ is the fraction of protonated or deprotonated species and n is the Hill coefficient. The Hill coefficient is a stretch parameter used to incorporate non-ideality into fits of the titration data[49] and is a positive (negative) number when monitoring the state of protonated (deprotonated) species. For solution titrations, $|n|$ should be close to its ideal value of one, with non-idealities often taking the form of $|n| < 1$. The pK_a value was calculated as the average of the pH values for the protonated and deprotonated species at θ = 0.5, which are the inflection points of the titration curves. The pK_a value for **1** dissolved in aqueous buffered solutions is similar to values reported for hydroxyl groups on tris(sulfonamide) pyrenols[50] and therefore is assigned to deprotonation of the hydroxyl group of **1**. Absorption spectral changes associated with this (de)protonation reaction were completely reversible as a function of pH and isosbestic points were maintained for all pH values reported. Three less acidic pK_a values for **1** dissolved in aqueous buffered solution with 100 mM KCl were determined to be ~8.6, ~10.5, and ~12.3 (Figures 1C and 1D) and are assigned to deprotonation of the three ammonium functional groups of **1**. Absorption

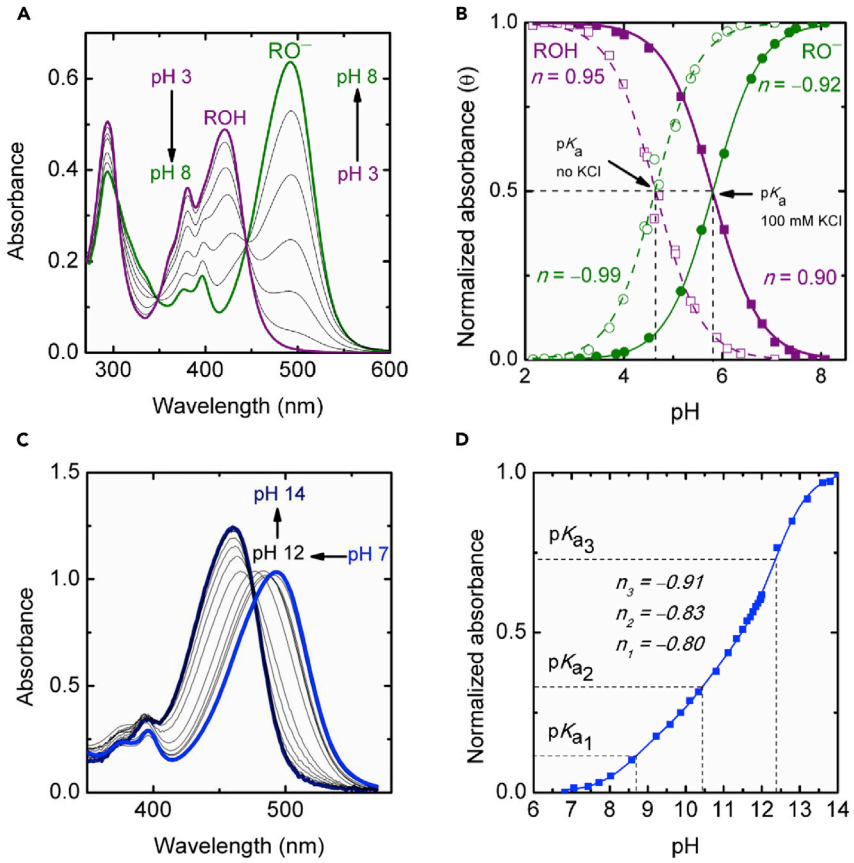

Figure 1. Ground-State Acidity of Photoacids from pH Dependence of Absorption Spectra

(A) Electronic absorption spectra of **1** dissolved in an aqueous buffered solution with 100 mM KCl at different pH values. Spectra of the ground-state species in their completely protonated (ROH) and deprotonated (RO^-) forms are bolded and colored.

(B) Plot of normalized absorbance (θ) at λ_{max} for each species (421 nm and 492 nm) as a function of pH and displayed with non-linear least-squares best fits to Equation 1. Also shown are the same types of plots and best fits for **1** dissolved in aqueous 1 mM KH_2PO_4 in the absence of supporting electrolyte and buffer, taken from Figure S1.

(C) Electronic absorption spectra over the indicated pH range of 7–14 with spectra of the ground-state species in their protonated and completely deprotonated forms bolded and colored.

(D) Plot of normalized absorbance (θ) at 460 nm (deprotonated species) as a function of pH and displayed with a non-linear least-squares best fit to a linear combination of three Hill equations (see Equation S1).

See also Figures S1, S3, S4, and S10, Table S1, and Supplemental Experimental Procedures, Determination of pK_a Values.

spectral changes associated with these reactions were also completely reversible as a function of pH. However, isosbestic points were not maintained at pH > 8 because of the similarity in the pK_a values, and therefore overlaps, in their titration events. When the aqueous electrolyte had lower buffering capacity with no additional supporting electrolyte, screening of charge by the electrolyte was diminished and the pK_a of the hydroxyl on **1** was observed to be ~4.6 (Figure 1B). This pK_a value is more than one unit smaller than the pK_a value for **1** dissolved in aqueous buffer containing supporting electrolyte (Figure 1). The *increased* acidity of **1** in the absence of supporting electrolyte is likely due to the presence of a *smaller* net positive charge on the conjugate base of **1**, and therefore, a greater relative stabilization of the deprotonated conjugate-base form of the photoacid. This is consistent with the

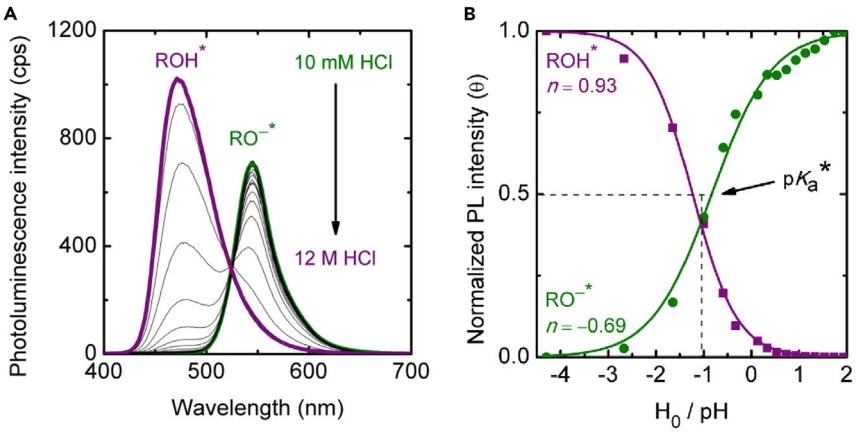

Figure 2. Excited-State Photoacidity of Photoacids from pH Dependence of Photoluminescence Spectra

(A) Photoluminescence (PL) spectra of **1** dissolved in different concentrations of aqueous HCl and using an excitation wavelength (λ_{ex}) of 379 nm. Spectra from the excited-state species in their completely protonated (ROH*) and deprotonated (RO^-*) forms are bolded and colored.

(B) Plot of normalized PL intensity (θ) at λ_{max} for each species (476 nm and 545 nm) as a function of Hammett acidity (H_0), for >1 M HCl, and pH, <1 M HCl, and displayed with non-linear least-squares best fits to Equation 1.

See also Figures S2–S4, Table S1, and Supplemental Experimental Procedures, Correction of Observed Photoluminescence Data.

behavior observed previously for 8-hydroxypyrene-1,3,6-trisulfonate, where its conjugate base has a *larger* net negative charge and therefore its acidity *decreased* when a lower concentration of supporting electrolyte was present in the aqueous solution.[51]

The excited-state pK_a, pK_a*, of **1** dissolved in acidic aqueous solution was estimated to be −1.1 via the Förster cycle analysis (Equation 2; see Figures S2–S4 and Supplemental Experimental Procedures, Correction of Observed Photoluminescence Data and Determination of pK_a* Values by Förster Cycle Analysis) as follows:

$$pK_a^* = pK_a - \frac{N_A hc(\nu_{ROH} - \nu_{RO^-})}{(\ln 10)RT}, \qquad \text{(Equation 2)}$$

where N_A is the Avogadro constant (6.022 × 10^{23} molecule mol^{-1}), h is the Planck constant (6.626 × 10^{-34} J s), c is the speed of light in vacuum (2.998 × 10^8 m s^{-1}), ν_{ROH} and ν_{RO^-} are the energies of the 0-0 electronic transitions of ROH and RO^-, respectively, and are expressed in units of inverse meters (m^{-1}), R is the ideal gas constant (8.314 J mol^{-1} K^{-1}), and T is the temperature (room temperature, 298.15 K). This analysis results in an approximation of the change in acidity between the equilibrated ground state and the thermally equilibrated excited state.[52,53] The pK_a* value approximated by the Förster cycle analysis was further corroborated by an experimental acid–base titration procedure with photoluminescence (PL) detection after appropriate corrections to the data (Figure 2; see Figure S2 and Supplemental Experimental Procedures, Correction of Observed Photoluminescence Data). Over the range of reported pH values, the hydroxyl group of **1** remained protonated while **1** was in its ground state (ROH). Under strongly acidic conditions, PL occurred exclusively from the protonated excited-state species (ROH*); however, at intermediate pH values, excitation (ex) of ROH resulted in emission (em) predominantly from the deprotonated excited-state species (RO^-*), which is indicative of excited-state proton transfer occurring within the lifetime of the excited state. After

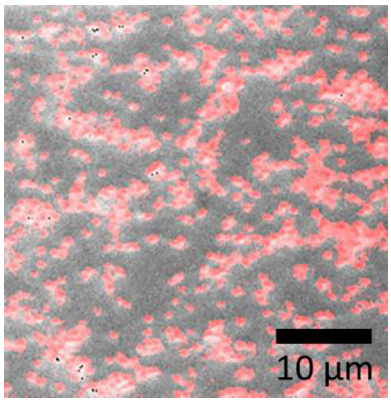

Figure 3. Microscopy Image of Porous Polymer Indicating Photoacid Localization in Pores

Optical microscopy reflection image of PET_8/**1** immersed in aqueous pH 3 solution (gray color gradient showing height topography), overlaid with emission from **1** (red) resulting from two-photon absorption (λ_{ex} = 900 nm). PL intensity from **1** was greater than PL intensity from the PET polymer. The optical microscopy image alone is shown as Figure S5 and clearly depicts the large base opening of the pores (dark spots, base side) that would be directly underneath the PL observed here. See also Figure S5.

conversion of negative pH values to Hammett acidity (H_0) values, the observed excited-state Hammett acidity value, $H^*_{0_{obs}}$, was determined to be −1.0 from a non-linear least-squares best fit of the corrected PL titration data to the Hill equation (Equation 1). The $H^*_{0_{obs}}$ value includes corrections for differences in the rates of excited-state decay of the emitting species, i.e., ROH* and RO^-*, back to ground state,[54] which is necessary because PL measurements occur under non-equilibrium conditions, and therefore, PL titration data do not provide a direct measurement of equilibrium pK_a* values. Assuming that the excited-state species reach a quasi-equilibrium, which is not always true especially for photoacids with short-lived excited states,[55] the actual pK_a* can be calculated from the observed pK_a* by correcting for the lifetime of each excited-state species as follows:[54]

$$pK_a^* = pK_{a_{obs}}^* + \log\left(\frac{\tau_{ROH}*}{\tau_{RO^-}*}\right), \qquad \text{(Equation 3)}$$

where τ stands for the lifetime and $pK_{a_{obs}}^*$ is the pH value at which $\theta = 0.5$. The lifetimes of ROH* and RO^-* for **1** were determined to be 3.9 ns and 5.8 ns via fluorescence lifetime imaging, respectively. The analogous equation using H_0^* values and Equations 3 and S3 follow,

$$H_0^* = \left(\frac{\tau_{RO^-}*}{\tau_{ROH}*}\right)\left(H^*_{0_{obs}} - 0.094\right) + 0.094. \qquad \text{(Equation 4)}$$

Using Equation 4, H_0^* was determined to be -1.6 ± 0.1, which is similar to the value of pK_a* obtained via the Förster cycle analysis (Equation 2), i.e., −1.1, and H_0^* values reported for analogous tris(sulfonamide) pyrenols.[50]

Functionalization of Polymer Pores with Photoacids

Conical nanopores in PET films were etched using a previously reported track-etching procedure,[56–58] with minor modifications. Briefly, heavy-ion irradiation of PET resulted in between 1 and 100,000,000 latent tracks per cm^2 that were then anisotropically chemically etched using a concentrated aqueous alkaline solution to yield conical nanopores. 1-Ethyl-3-(3-dimethylaminopropyl)carbodiimide was employed to covalently anchor **1** to the inside of the conical nanopores to yield a PET_n/**1** film, where 10^n is the projected areal coverage of nanopores in units of pores cm^{-2}. 15 single conical nanopores (15 PET_0) were calculated to have large base openings with diameters of approximately 200–500 nm (400 ± 90 nm, as the mean ± standard deviation) and small tip openings with diameters of approximately 1–17 nm (4 ± 4 nm). Base diameters were estimated on the basis of bulk etching rates, and tip diameters were estimated on the basis of the resistance of the pores immersed in aqueous 1 M KCl, according to a previous literature procedure.[58]

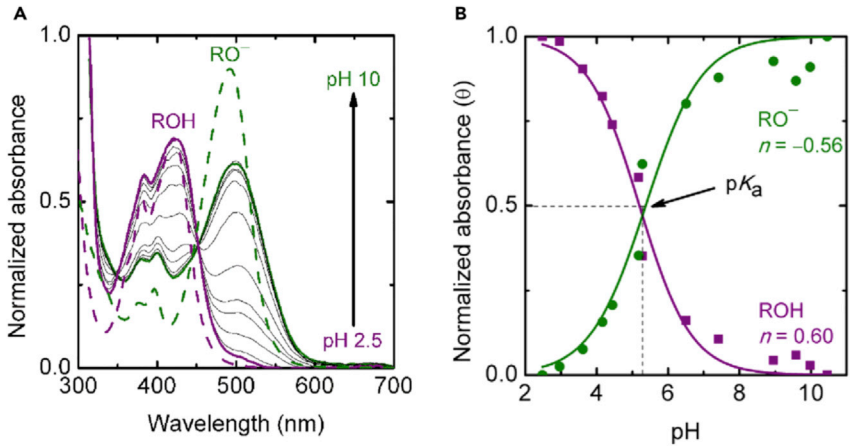

Figure 4. Ground-State Acidity of Polymer-Bound Photoacids from pH Dependence of Absorption Spectra

(A) Electronic absorption spectra of PET_8/**1** wetted with aqueous buffered solutions at different pH values. Spectra of the ground-state species in their completely protonated (ROH) and deprotonated (RO^-) forms are bolded and colored, and spectra from Figure 1A of **1** dissolved in an aqueous buffered solution are shown as dashed lines with the same colors.

(B) Plot of normalized absorbance (θ) at λ_{max} for each species (426 nm and 498 nm) as a function of pH and displayed with non-linear least-squares best fits to Equation 1.

See also Figures S1, S3, S10, and S11 and Table S1.

Localization of **1** within PET pores was supported by data from two-photon fluorescence microscopy of PET_8/**1** (Figure 3; see Figure S5), cyclic voltammetry of PET_n with and without **1** bound resulting in variations in ion selectivity and buffering capacity (see Figures S6–S8; Table S2; Text S1, Current Understanding of the Electrochemical Response of Nanopores), and experimental determination of surface binding coverage in PET_8/**1** (see Figure S9; Table S3; Supplemental Experimental Procedures, Estimation of Binding Coverage of Photoacids in Nanopores). Two-photon fluorescence microscopy allowed selective excitation of photoacids bound in the pores and emission was clearly observable from regions coincident with pores. However, this technique did not afford information on the chemical identity of the bound species. Compound **1** has three free primary amine functional groups that can be covalently linked to PET through carboxylates to form up to three amide linkages. Knowing the approximate number of amide linkages formed between **1** and PET provides a more complete picture of the electrostatic and chemical environment in PET_n/**1**, which is described below.

PET_8/**1** has maximum absorbance values at 426 nm and 498 nm and all major absorption peaks exhibited ~5 nm bathochromic shifts as compared to those observed for **1** in solution (Figure 4A). Across the pH range tested, changes in absorption were consistent with data in solution for deprotonation of the hydroxyl group of **1**, which suggest that **1** did not bind to PET through the hydroxyl group (Figure 4). Hypsochromic shifts that accompanied deprotonation of ammonium groups on **1** in solution (Figure 1C) were not observed for PET_8/**1** when immersed in an aqueous solution at pH 8–10.5. This suggests that ammonium groups in PET_8/**1** were not deprotonated across this pH range tested, even though pK_a values of these ammonium groups observed for **1** in solution were 8.6, 10.5, and 12.3 (Figure 1D). These data suggest that at least the two most acidic ammonium groups of **1** reacted with PET to form covalent bonds and/or that the pK_a values for unreacted ammonium groups are >~12. A summary of the photophysical and photochemical properties of **1** and PET_8/**1** are presented in Table S1.

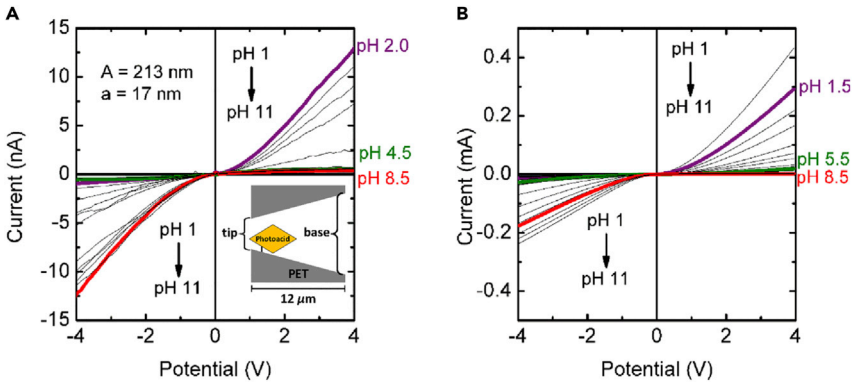

Figure 5. Ground-State Acidity of Polymer-Bound Photoacids from pH Dependence of Cyclic Voltammograms

Cyclic voltammograms of (A) PET_0/**1** and (B) PET_8/**1** immersed in aqueous 100 mM KCl solutions at different pH values. The calculated diameters of the large base opening (A) and the small tip opening (a) are also shown, as well as a schematic of the nanopore as an inset.
See also Figure S6.

Measurement of Ground-State Acidities of Polymer-Bound Photoacids

For photoacid-functionalized nanopores to serve as efficient light-driven ion pumps, PET_n/**1** should be a weak acid in its ground state and a strong photoacid in its excited state. For PET_8/**1** immersed in an aqueous buffered solution, $pK_a = 5.1 \pm 0.2$ for the hydroxyl group of **1** as determined by an acid–base titration procedure with spectrophotometric detection (Figure 4). This value is 0.7 pH units more acidic than the pK_a of the hydroxyl group of **1** when dissolved in solution but is consistent with the pK_a value of ~5.4 observed for a model of PET_n/**1**, i.e., tris(methylterephthalate)-capped **1** (photoacid **2**), in aqueous solution containing no intentional inert electrolyte salt (see Figure S10; Scheme S1). These data support that terephthalate polymer units stabilize the conjugate base of **1**, which is similar to the stabilization effects lysozymes have on 8-hydroxypyrene-1,3,6-trisulfonate via hydrogen bonding, van der Waals interactions, and electrostatic interactions.[51] The large degree of non-ideality observed in the acid–base titration data for PET_8/**1** ($|n|$ = 0.55–0.60) is most likely caused by a distribution of pore sizes and/or nanoenvironments that are not present when **1** is dissolved in solution.

The acid–base titration procedure with spectrophotometric detection reported on the average pK_a of all photoacid molecules bound to the PET surface but did not provide information about the pK_a of photoacids bound specifically in the tips of the nanopores. The tip region is reported to have a small built-in electrostatic potential,[23–25,59–63] and therefore is a major contributor to the observed ionic current rectification behavior, suggesting that photoacids in this region may be more likely to facilitate ionic photovoltaic action. Because the net charge in the tip of a nanopore affects its ionic current–potential behavior, cyclic voltammetry as a function of solution pH of PET_0/**1**, and PET_8/**1** in order to make a direct comparison to the data in Figure 4, were used to assess the net charge in the tips of nanopores (Figure 5).[26,58,64–66] Under acidic conditions (pH 1.5–2.0), current rectification consistent with a net positively charged tip of PET_n/**1** was observed. This behavior strongly suggests that at least some of **1** are covalently bound in the tip of the nanopore, each with at least one free cationic ammonium group and a neutral hydroxyl group. As the pH was titrated to more basic values (pH 2.0–5.5), the current–potential response became ohmic and highly resistive. This behavior occurred at pH values smaller than those measured during deprotonation of the hydroxyl group of **1** bound

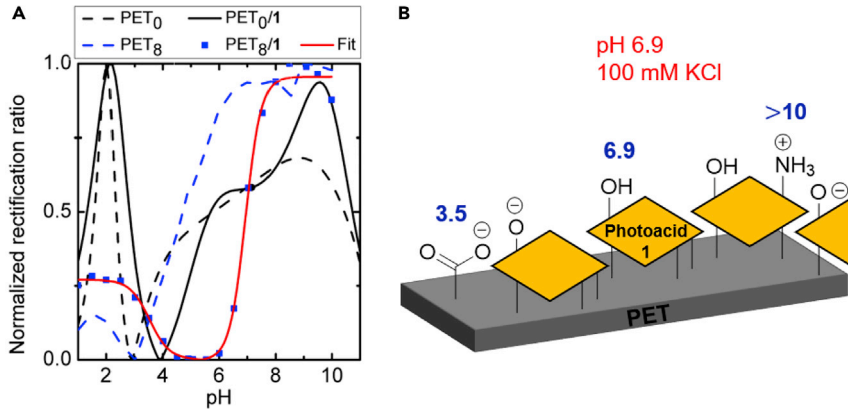

Figure 6. Distribution and Binding Mode of Polymer-Bound Photoacids from pH Dependence of Rectification Ratio

(A) Rectification ratio values as a function of pH for PET_n immersed in aqueous 100 mM KCl solutions.

(B) Representative arrangement of species in the modified tip region of PET_8/**1** at pH 6.9 based on values obtained from non-linear least-squares best fit of the PET_8/**1** data in (A) to Equation S1. Blue colored numbers located above functional groups correspond to their approximate pK_a values obtained from inflection points of the best-fit curve. The *n* values for the non-linear least-squares best fit to Equation S1 are listed in Table S2.

See also Figures S6–S9 and Tables S2 and S3.

to PET_8/**1** (Figure 4), and therefore, this process is reasonably ascribed to deprotonation of unreacted terephthalic acid groups in the tip of the nanopore, which aided in charge neutralization of the ammonium groups. Upon further titration of the pH toward more alkaline conditions (pH 5.5–10) current rectification returned but this time the behavior was consistent with a net negatively charged tip of the nanopore, likely caused by deprotonation of the hydroxyl group of **1**. These positive–neutral–negative surface features were consistently observed during the titration of another eleven individual PET_0/**1** (see Figure S6).

The titration data were further analyzed to determine pK_a values and the binding mode and binding coverage of **1** to the nanopore surface. Consistent with protocols in previous reports, extreme current values at $\pm$4 V (see Figure S8) were converted into rectification ratios, normalized, and plotted as a function of pH (Figure 6A).[66–70] Data obtained from PET_0/**1** lacked the sigmoidal character expected for this analysis, likely because a single nanopore does not have a sufficient ensemble of molecules required for accurate fits to the Hill equation (Equation 1). Instead, data from the ensemble of pores in PET_8/**1** were best fitted to a linear combination of three Hill equations (see Equation S1). Three Hill equations were required to account for changes in surface charge due to deprotonation of carboxylic acid, hydroxide, and primary ammonium moieties (Figure 6). Inflection points of the best-fit curve to the rectification ratio data likely represent pK_a values of functional groups that line the inside tips of the nanopores. The pK_a values were approximated to be ~3.5, ~6.9, and >10 and were attributed to the carboxylic acid, hydroxyl, and ammonium moieties, respectively. The ammonium pK_a value could not be measured accurately because at pH > 10 the PET polymer undergoes significant hydrolysis. Rectification ratio values close to unity are consistent with conditions where there is a nearly spatially invariant net charge of zero at the tips of the nanopores. The pH values corresponding to this condition are termed isoelectric points and are equal to the pH values corresponding to minimum values of the normalized rectification ratio (Figure 6A). The isoelectric points of native PET_0 and PET_8 were

Table 1. Acidities and Photoacidities of Photoacids

Sample	1	PET_8/1		
[aq. KCl] (M)	100	100	100	0
Region Probed	dissolved photoacid	nanopore tip	entire film	nanopore tip
pK_a	5.80 ± 0.03[a]	6.9[d]	5.1 ± 0.2[a]	–
pK_a* (H_0^*)	−0.65 ± 0.02[b] (−1.6 ± 0.1)[b] −1.1[c]	0.2[e] −1.4[c]	–	1.4[e]

Ground-state and excited-state pK_a values for the hydroxyl group of **1** and PET_n/**1**. See also Figures S4 and S11 and Table S2.

[a]Determined from absorption titration data and Equation 1.

[b]Determined from photoluminescence titration data, λ_{ex} = 379 nm, and Equations 1, 3, and 4.

[c]Determined using the Förster cycle analysis and Equation 2.

[d]Determined from cyclic voltammetry titration data and Equation 1.

[e]Determined from two-photon PL microscopy, λ_{ex} = 900 nm, and Equations 1, 3, and 4.

determined to be 3.0, which is consistent with previous reports.[58,71] After modification with **1**, the average isoelectric point of PET_0/**1** shifted slightly more basic to 3.9, and the isoelectric point of PET_8/**1** shifted even farther to a range of 4.5–6. This large uncertainty in the isoelectric point likely resulted from an ensemble of nanoenvironments and/or distribution of pore sizes. These changes in isoelectric point strongly suggest that the surface of the nanopore was substantially modified. Similar changes in buffering capacities of covalently modified PET nanopores have been extensively documented, and some exemplary modifications include amino acids[66,72] and ionic polymers.[67,68,73]

Based on the best-fit weightings for each Hill equation of 0.27, 0.96, and 0.27, respectively (see Table S2), the total number of carboxylic acids and primary ammoniums were determined to be approximately equal and with 3.6 times more hydroxyls (3.6:1:1 ROH: $R'NH_3^+$ R″COOH). Because each photoacid molecule has three amines and one hydroxyl and data support that no hydroxyls were covalently bonded to PET, this implies that for every 10.8 amines on **1** (3.6 × 3) one amine did not react with PET. Therefore, 91% of the amines on **1** reacted with 91% of the carboxylic acids on the surface of the PET nanopores ([10.8 − 1]/10.8) to covalently bond photoacids to PET. Furthermore, because, on average, each molecule of **1** was bound to ~2.7 carboxylates on PET (3 × 0.91) and native PET nanopores have ~1 COOH nm^{-2},[64] the binding coverage of **1** was ~0.4 nm^{-2} (1/2.7). This value was further substantiated by results from a two-step coupling–hydrolysis procedure (see Figure S9; Table S3; Supplemental Experimental Procedures, Estimation of Binding Coverage of Photoacids in Nanopores). A summary of the pK_a values measured in this work is presented in Table 1. Collectively, these data suggest that the pK_a value of the hydroxyl group of **1** is most basic when **1** is bound in the tip of the nanopore (pK_a ≈ 6.9), followed by when **1** is dissolved in an aqueous solution (pK_a ≈ 5.8) and is most acidic when **1** is tris(methylterephthalate) capped (as photoacid **2**) and dissolved in an aqueous solution (pK_a ≈ 5.4) or **1** is bound to bulk PET polymer (pK_a ≈ 5.1). The observed ~2 pH unit shift in the pK_a value of the hydroxyl group of **1** when bound in the tip of a PET nanopore is consistent with an electrostatic perturbation arising from a ~100 mV potential drop (~2 × 2.303RT/F). This calculated potential drop is similar to values that were previously reported in the literature for the potential drop in the tips of PET nanopores.[25,74] Moreover, this general observation and hypothesis are consistent with those proposed to occur in related systems containing amino acids[66,72] and ionic polymers[67,68,73] where, as dictated by the Poisson equation, changes in local charge distributions alter local

electric fields, local electric potentials, local internal chemical energies, and, therefore, local chemical equilibria. For Brønsted acidity, this means that the value of K_a, and therefore pK_a, differs from its value in the absence of these altered charge distributions. In addition, given the approximate net charge density of the tip of a nanopore modified with **1** (Figure 6B), the observed shift in pK_a to less acidic values is consistent with a condition where less salt resides in the tip of the nanopore, as discussed in relation to the shift in pK_a of **1** dissolved in an aqueous solution containing minimal buffer and no supporting electrolyte (Figure 1B) and analogous photoacid molecules.

Measurement of Excited-State Photoacidities of Polymer-Bound Photoacids

Fluorescence-lifetime imaging microscopy was used to measure the excited-state lifetime of PET_8/**1** immersed in concentrated aqueous HCl and an aqueous pH 10 solution. The measured excited-state lifetimes were 1.0 ns for ROH* and 1.2 ns for RO^-*, which are shorter than the excited-state lifetimes of ROH* and RO^-* for **1** dissolved in an aqueous solution (3.9 ns and 5.8 ns, respectively). These differences in lifetime suggest that when **1** is bound to PET, additional and/or faster non-radiative relaxation pathways are likely operative.

Measurement of pK_a* in the nanopores requires that only the tip of the nanopores be functionalized because emission from other regions of the polymers convolute the signal. To locate **1** specifically in the tips of the nanopores, taurine (T) was used to cap free carboxylates on the outward-facing surface of PET on the side with the small nanopore tip opening so that they would be unreactive (PET_8/T). Similar to the solution studies, the Förster cycle analysis (Equation 2) suggested that pK_a* = −1.4 in PET_8/T+**1** (see Figure S11), which is consistent with pK_a* calculated by the same method for **1** dissolved in an aqueous solution (pK_a* = −1.1). Also analogous to **1** in solution, PET_8/T+**1** that contained ROH species and immersed in weakly acidic aqueous solutions exhibited PL from RO^-* species (Figure 7), indicating that **1** underwent excited-state proton transfer and therefore was a photoacid when covalently bound to the tip of a PET nanopore. However, under these weakly acidic conditions, PL from ROH* was also observed for PET_8/T+**1**, which is in contrast to that expected based on the PL spectra of **1** dissolved in an aqueous solution and the results from the simple Förster cycle analysis. For instance, for PET_8/T+**1** at pH 3, ~40% of the emission was from ROH* (Figure 7; see Figure S12) whereas for **1** in solution, >99% of the emission was from ROH* (Figure 2). Also, results from an acid–base titration procedure with photoluminescence PL detection indicate that in contrast to the H_0^* value of **1** dissolved in solution (H_0^* = –1.6), PET_8/T+**1** exhibited pK_a* = 1.4 in the absence of supporting electrolyte (Figure 7B; Equation 3) and pK_a* = 0.2 in the presence of 100 mM KCl supporting electrolyte (Figure 7D; Equation 3). This suggests that surface attachment of **1** to PET and/or nanoconfinement alters the observed value of pK_a*. PL spectra were completely reversible as a function of pH and isoemissive points were maintained for all pH values reported. A summary of the pK_a* values measured in this work is also included in Table 1.

To rationalize the observed excited-state behavior, several hypotheses were evaluated. One hypothesis was that under focused laser excitation, the local steady-state concentration of protons was greatly increased in comparison to the concentration at equilibrium in the dark. To assess this hypothesis, PL from PET_8/T+**1** immersed in an aqueous pH 3 solution was measured as a function of excitation laser irradiance. Only minor changes corresponding to a relative decrease in ROH* emission were observed for nearly an order-of-magnitude increase in laser irradiance (see Figure S13), suggesting that this was not the cause of the observed excited-state

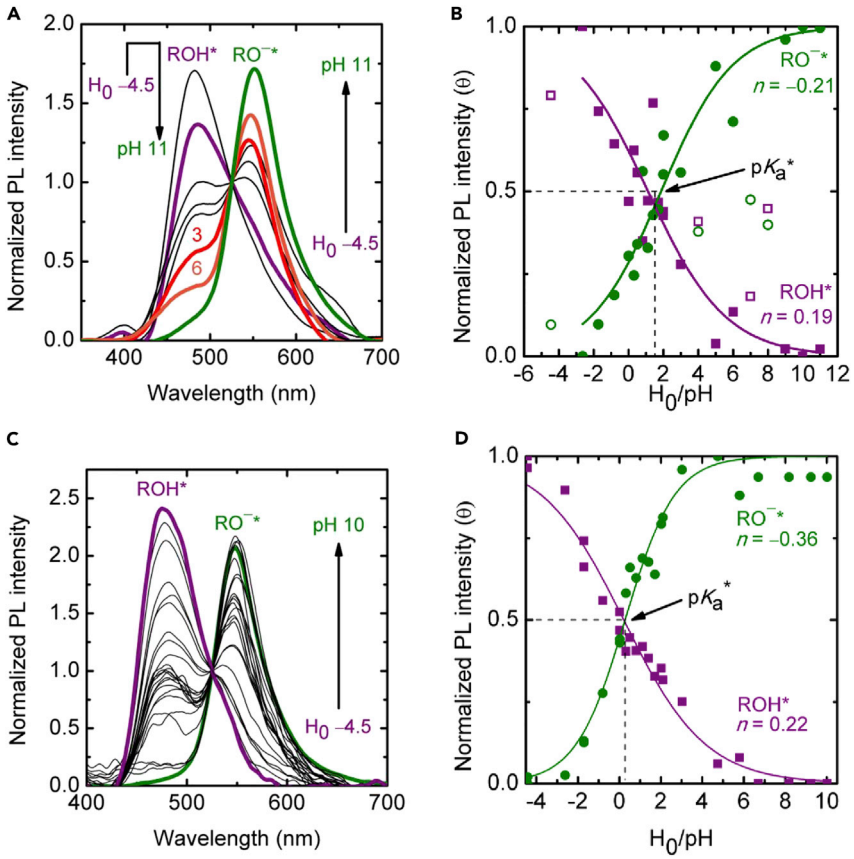

Figure 7. Excited-State Photoacidity of Polymer-Bound Photoacids from pH Dependence of Photoluminescence Spectra

(A) Photoluminescence (PL) spectra of PET_8/T+**1** immersed in aqueous solutions at different Hammett acidity (H_0) or pH values and excited with a two-photon-absorption wavelength (λ_{ex}) of 900 nm. Spectra from the excited-state species in their completely protonated (ROH*) and deprotonated (RO^-*) forms are bolded and colored.

(B) Plot of normalized PL intensity (θ) at λ_{max} for each species (479 nm and 548 nm) as a function of H_0 for >1 M HCl and pH for <1 M HCl, and displayed with non-linear least-squares best fits to Equation 1, after excluding the data points shown as unfilled shapes.

(C) PL spectra of PET_8/T+**1** immersed in aqueous 100 mM KCl solutions at different H_0 or pH values and excited with λ_{ex} = 900 nm. Spectra from the excited-state species in their completely protonated (ROH*) and deprotonated (RO^-*) forms are bolded and colored.

(D) Plot of normalized PL intensity (θ) calculated from full spectral modeling[55] as a function of H_0 for >1 M HCl and pH for <1 M HCl, and displayed with non-linear least-squares best fits to Equation 1.

See also Figures S2, S3, and S11–S13; Tables S1 and S4; Supplemental Experimental Procedures, Correction of Observed Photoluminescence Data and Determination of Excited-State pK_a Values in Polymers.

behavior. Another hypothesis is that differing electrostatic regions in the nanopores resulted in a local environment with more or less of a specific type of ion, including protons, as compared to the bulk solution. This is reasonable given that pK_a* decreased in the presence of supporting electrolyte (Figures 7C and 7D) likely due to additional screening of surface charges, which altered the local electrostatics and/or the local pH of the nanopores. Moreover, both pK_a and H_0^*/pK_a* for the hydroxyl group of **1** increased by ~1 pH unit when bound to PET in the tip of the nanopore in comparison to values measured when **1** was dissolved in solution. A final hypothesis is that nanoconfinement alters pK_a values due to slow hydrogen bond dynamics that prevent water molecules from optimally solvating RO^-* and H^+ formed

from the excited-state proton-transfer step.[75,76] This would result in a shift in the excited-state quasi-equilibrium toward the protonated species and a decrease in the yield for net proton transfer,[77–79] which would be manifest as an increase in the observed value of pK_a*. Irrespective of the mechanism, **1** is a weaker photoacid when bound to the tip of hydrated charged PET nanopores.

Recent studies by White et al. suggest that when photoacid-modified Nafion is illuminated with visible light, ionic photovoltaic action is observed.[37,39] However, the photocurrent was at least in part limited by an increase in pK_a* for dyes bound in the nanopores of Nafion versus values measured when dissolved in an aqueous solution.[37,48] The nanopores reported herein are nearly ideal models for these materials because the diameters of the nanopore tips are on the same sub-10-nm size scale as hydrated domains in Nafion.[37,39] While photocurrents from modified PET nanopores have been previously reported,[80,81] we were not able to measure reliable photocurrents and photovoltages from our materials under any conditions, which we expected to be the case based on the absorption spectra and photophysical properties of our materials. Nevertheless, our results above suggest that the values of pK_a and pK_a* for **1** bound to the nanoporous tip region of PET become less acidic. This increase in pK_a* is undesired for the ultimate application of these materials and suggests that alternative photoacids with more negative values of pK_a* or ion-exchange materials with more alkaline local pH will likely be required in order to realize an effective combination of molecules and materials that results in large yields for light-to-ionic energy conversion. Studies are currently underway to assess the feasibility of using membranes and/or nanopores with altered surface chemistries and/or using photoacids with more acidic pK_a* values, with larger magnitudes of ΔpK_a, and/or that prefer to be localized in the center of nanochannels where the characteristics of water more closely resemble that of bulk water.[75]

Conclusions

Water-soluble photoacid molecules with terminal ammonium groups were synthesized. The terminal ammonium groups allowed for facile coupling to carboxylic acids on nanoporous PET surfaces. Spectrophotometric titration curves showed that the hydroxyl pK_a of photoacid **1** was 5.8 when dissolved in an aqueous solution. When **1** was covalently linked to PET nanopores, electrochemical measurements and electronic absorption spectroscopy data suggest that the hydroxyl pK_a of **1** was 5.1 and increased to 6.9 in the confined tip of the nanopore. This increase in pK_a is consistent with behavior expected when ions are excluded from the tip of the nanopore and a larger potential affects surface-confined **1**. Also, a majority of **1** were attached to PET nanopores via all three of their amine groups, the PET surface was ~90% modified, and **1** had a binding coverage of ~0.4 photoacids nm^{-2}. Förster cycle analyses and PL titration measurements indicated that the hydroxyl pK_a* of **1** in aqueous solution was approximately −1. Fluorescence microscopy was used to show that **1** bound to PET was localized within nanopores and **1** still operated as a photoacid. The apparent pK_a* was 0.2 when PET$_8$/**1** was immersed in aqueous 100 mM KCl and was less acidic when no supporting electrolyte was present. Moreover, titration curves of PET$_n$/**1** were highly non-ideal, which was postulated to be due to an aggregate of confinement effects, a distribution in pore geometries, and differences in nanoenvironments. Additionally, the excited-state lifetime of **1** significantly decreased from about 4–5 ns to ~1 ns upon binding to PET. These observations suggest that less acidic environments are needed to observe excited-state proton transfer in small nanopores with tip diameters < 10 nm. Use of these materials for application in light-driven proton pumps requires further advances but could conceivably be improved by incorporating different photoacids and/or membranes.

EXPERIMENTAL PROCEDURES

General Synthetic Procedures

Unless otherwise stated, all reactions were perfromed under an inert atmosphere of nitrogen in oven-dried flasks equipped with Teflon-coated magnetic stir bars. All chemicals were obtained from commercial suppliers and used with no further purification. Reactions were monitored by time-of-flight mass spectrometry or by thin-layer chromatography using silica gel 60 F_{254} on aluminum sheets with ultraviolet light for visualization.

Reagents

Pyranine (>85%, TCI America), acetic anhydride (99%, EMD Millipore), sodium hydroxide (≥95%, Macron Fine Chemicals), potassium chloride (≥99%, Fisher Scientific), 1-(3-dimethylaminopropyl)-3-ethylcarbodiimide (EDC) hydrochloride (98%, Alfa Aesar), 1-boc-ethylenediamine (98%, Combi-Blocks), thionyl chloride (≥99%, Sigma-Aldrich), propylamine (98%, Sigma-Aldrich), ethylenediamine (99%, Acros Organics), 2-(*N*-morpholino)ethanesulfonic acid (MES) hydrate (99%, Oakwood Chemical), tris(hydroxymethyl)aminomethane (≥99.8%, Fisher Scientific), potassium phosphate monobasic (≥99.5%, Fisher Scientific), sodium tetraborate decahydrate (≥99.5%, Fisher Scientific), citric acid anhydrous (≥99.5%, Fisher Scientific), hydrochloric acid 36.5%–38% (EMD Millipore), trifluoroacetic acid (99%, Oakwood Chemical), formic acid (88%, Fisher Scientific), dimethylsulfoxide (≥99.9%, EMD Millipore), taurine (99%, Sigma-Aldrich), methylterephthalate (97%, Sigma-Aldrich), and *N*-hydroxysuccinimide (98% Sigma-Aldrich) were used.

Spectroscopic Characterization

Nuclear magnetic resonance (NMR) spectra were collected at 298 K at 400 MHz using a Bruker AVANCE400 spectrometer or at 500 MHz using a Bruker CRYO500 spectrometer (see Figure S14). Chemical shifts are reported using the standard δ notation in parts per million (ppm) relative to solvent peaks (^{1}H, ^{13}C). Peak multiplicities are listed as follows: s, singlet; d, doublet; t, triplet; q, quartet; and m, multiplet. The *J*-coupling constants are reported in Hertz. Infrared spectra were recorded on a Perkin-Elmer Spectrum One Fourier transform infrared (FTIR) spectrophotometer; samples were prepared as KBr pellets. Mass spectrometric data were collected for samples dissolved in methanol using liquid chromatography electrospray ionization time-of-flight mass spectrometry on a Waters Micromass LCT Premier mass spectrometer (see Figure S15).

Chemical Syntheses

Sodium 8-Acetoxypyrene-1,3,6-trisulfonate (E1)

Sodium hydroxide (0.80 g, 20 mmol) was added to a stirring solution of pyranine (9.59 g, 18 mmol) dissolved in water (10 mL). The solution was stirred for 15 min and then concentrated under vacuum to dryness. A heated water bath was used to assist the distillation process. Acetic anhydride (100 mL) was added. The suspension was heated to reflux and stirred for 14 h. A white powder was collected via filtration and washed with dichloromethane and acetone; the powder was dried under vacuum (10.7 g, 18 mmol, quantitative yield). ^{1}H NMR (500 MHz, D_2O) δ 9.24 (s, 1H), 9.23 (d, *J* = 10.0, 2H), 9.17 (d, *J* = 10.0, 1H), 9.13 (d, *J* = 9.5, 1H), 8.56 (s,1H), 8.51 (d, *J* = 9.5, 1H), and 2.65 (s, 3H); ^{13}C NMR (500 MHz, D2O) δ 173.4, 144.5, 138.3, 136.2, 136.1, 129.7, 129.0, 127.1, 126.4, 125.6, 125.5, 125.3, 125.0, 125.0, 124.7, 123.4, 120.2, and 20.5; FTIR (KBr pellet) ν 3,470 (st) cm^{-1}, 2,959 cm^{-1}, 1,736 (m) cm^{-1}, 1,569 (m) cm^{-1}, 1,206 (st) cm^{-1}, and 1,060 (st) cm^{-1}.

3,6,8-Tris(chlorosulfonyl)pyren-1-yl acetate (E2)

While stirring, pyrene **E1** (4.352 g, 7.684 mmol) was slowly added to a solution of thionyl chloride (10 mL) containing three drops of *N*,*N*-dimethylformamide. The reaction was refluxed for 5 h. The crude product was poured onto an aqueous ice slurry and dissolved with dichloromethane. The organic layer was separated and concentrated *in vacuo* to obtain a yellow powder (3.312 g, 5.400 mmol, 78%). ^{1}H NMR (500 MHz, $CDCl_3$) δ 9.68 (d, *J* = 10.0, 1H), 9.62 (s, 1H), 9.51 (d, *J* = 10.0, 1H), 9.45 (d, *J* = 9.7, 1H), 8.91 (s, 1H), 8.83 (d, *J* = 9.7, 1H), and 2.67 (s, 3H); ^{13}C NMR (500 MHz, $CDCl_3$) δ 168.7, 147.2, 140.8, 137.4, 137.2, 133.1, 131.9, 129.9, 128.2, 128.1, 127.6, 126.5, 126.1, 125.5, 125.4, 124.7, 123.4, and 21.3.

Tert-butyl-(2-((6,8-bis(N-(2-((tert-butoxycarbonyl)amino)ethyl)sulfamoyl)-3-hydroxypyrene)-1-sulfonamido)ethyl)carbamate (E3)

N-boc-ethylenediamine (4.5704 g, 28.52 mmol) was added to a solution of H_2O (2 mL), tetrahydrofuran (4 mL), and acetonitrile (14 mL). While stirring, pyrene **E2** (2.184 g, 3.938 mmol) was added. An additional solution of H_2O (2 mL), tetrahydrofuran (4 mL), and acetonitrile (14 mL) was added. The resulting red-violet solution was stirred for 19 h at room temperature. Consequently, NaOH pellets (0.3 g) were added to the mixture and stirred for 2.5 h before additional NaOH pellets (0.4 g) were added. After 1.5 h, 100 mL of chloroform and 100 mL of 1 M NaOH were added and vigorously shaken (with occasional venting) until the red product dissolved completely into the aqueous layer. The aqueous solution was washed with chloroform (200 mL × 4). The aqueous layer was separated, ice was added directly to the solution, and then acidified with a chilled solution of HCl (concentrated HCl was added directly to the ice in a 1:3 volume ratio). The resulting yellow precipitate was collected via vacuum filtration and dried under vacuum (3.224 g, 3.643 mmol, 92%). ^{1}H NMR (500 MHz, CD_3OD) δ 9.21 (s, 1H), 9.18 (d, *J* = 9.8, 1H), 8.90 (d, *J* = 9.6, 1H), 8.94 (d, *J* = 9.8, 1H), 8.80 (d, *J* = 9.6, 1H), 8.30 (s, 1H), 2.98 (coalescing m, 12H), and 1.15 (coalescing s, 27H).

2,2′,2′′-((8-Hydroxypyrene-1,3,6-trisulfonyl)tris(azanediyl))tris(ethan-1-aminium) tris(trifluoroacetate) (1)

Trifluoroacetic acid (10 mL) was diluted with dichloromethane (50 mL) and then chilled on ice. Pyrene **E3** (3.088 g, 3.489 mmol) was then added to the chilled solution, which was then removed from the ice and stirred for 1 h. The reaction mixture was concentrated *in vacuo*. Residual trifluoroacetic acid was co-distilled with 5 × 20 mL dichloromethane and the resulting orange powder was dried further under high vacuum. For further purification, the powder was dissolved in a solution of 1:19 CH_3CN:H_2O (v/v) spiked with 0.1% trifluoroacetic acid. The solution was passed through a 0.2 μm filter and then injected into a preparatory reverse-phase high-performance liquid chromatography instrument where the gradient was set from 5% CH_3CN (aq, 0.1% trifluoroacetic acid) to 90% CH_3CN (aq, 0.1% trifluoroacetic acid) over 30 min. The flow rate was set to 15 mL/min. Pyrene **1** was collected from 15% to 33% CH_3CN. Note that the preparatory reverse-phase high-performance liquid chromatography instrument used has a maximum capacity of ∼0.8 grams of solute; therefore, the product was divided into 4 equal portions, each less than 0.8 grams. Each portion was dissolved in 4.5 mL of the solution of 1:19 CH_3CN:H_2O (v/v), and a total of 4 runs were made to collect the entire batch of product. The desired fractions were concentrated *in vacuo* to obtain a yellow solid (3.201 g, 3.454 mmol, 99%).^{1}H NMR (600 MHz, DMSO-D_6) δ 9.19 (d, *J* = 9.7, 1H), 9.15 (s, 1H), 9.02 (d, *J* = 9.6, 1H), 8.92 (d, *J* = 9.7, 1H), 8.84 (d, *J* = 9.6, 1H), 8.76 (broad, 1H), 8.69 (broad, 1H), 8.66 (broad, 1H), 8.41 (s, 1H), 7.90 (broad, 9H), 3.07 (broad q, *J* = 5.9, 2H), 3.01 (broad m, 4H), 2.86 and 2.84 (coalescing, 6H); ^{13}C NMR (600 MHz,

DMSO-D_6) δ 158.6 (q, *J* = 126, trifluoroacetate), 158.5 (q, *J* = 126, trifluoroacetate), 155.0, 136.9, 131.7, 130.5, 130.4, 130.3, 128. 6, 128.1, 126.2, 125.8, 125.5, 123.3, 121.2, 120.4, 118.4, 117.1 (q, *J* = 1188, trifluoroacetate), 117.1 (q, *J* = 1188, trifluoroacetate), 115.7, 40.0, 39.9, and 38.6. The *m/z* ratio for $[M+H]^+$ was calculated to be 585.1260 and was found to be 585.1270, with an acceptable Δ = 2.9 mDa, and an observed Δ = 1.0 mDa.

Electronic Absorption Characterization of 1 in Aqueous Buffered Solution

Equal amounts of **1** were portioned into three separate volumetric flasks of the same volume. Sodium tetraborate decahydrate (0.1 M), citric acid anhydrous (0.1 M), tris(hydroxymethyl)aminomethane (0.1 M), potassium phosphate monobasic (0.1 M), and potassium chloride (0.1 M) were added. The three flasks were filled with 12 M HCl, 2 M NaOH, and distilled water (weakly acidic) to the volumetric marker. Solutions were stirred until dissolved. The weakly acidic solution was titrated with the 12 M HCl or 2 M NaOH buffered solutions to reach the desired pH values from 2 to 12. The pH was measured using a Fisher Scientific pH/Ion 510. The pH meter does not accurately read pH values more acidic than pH 1 and more alkaline than pH 12. Therefore, solutions with pH values greater than 1 and more alkaline than 12 were made from the aliquots of the 12 M HCl and 2 M NaOH solutions, and the pH value was calculated based on the portioning. Ultraviolet–visible electronic absorption spectra were recorded on a Cary 60 UV-Vis Spectrophotometer. Samples consisted of aliquots dispensed in a quartz cuvette (1 cm pathlength) and were kept at room temperature. Spectra were subtracted by a blank buffering solution. The titration was performed four times in order to obtain the mean and standard deviation of the data. The procedure was also replicated using a less extreme buffer system that contained 1 mM potassium dihydrogen phosphate and no supporting electrolyte (see Figure S1).

Photoluminescence Characterization of 1 in Acidic Aqueous Solution

Equal amounts of **1** were portioned into two separate volumetric flasks. The two flasks were made to contain concentrated HCl and deionized water titrated with concentrated aqueous HCl to pH 3. Ultraviolet–visible electronic absorption spectra were recorded for both samples. Samples consisted of aliquots dispensed in a quartz cuvette (1 cm pathlength) and were kept at room temperature. The smallest difference in absorbance occurred at the wavelength of 379 nm and was 0.009 units, and thus 379 nm was chosen as the excitation wavelength for PL titration studies. Further samples were prepared by mixing the two solutions. A known volume of pH 3 solution was titrated using known volumes of concentrated aqueous HCl, which allowed the calculation of intermediate pH values. For each sample, an ultraviolet–visible electronic absorption spectrum and PL emission spectra were recorded. The ultraviolet–visible electronic absorption spectra were recorded on a Cary 50 Ultraviolet-Visible Spectrophotometer. PL emission spectra were recorded using a Cary Eclipse Spectrophotometer using the following excitation and emission parameters: λ_{ex} = 379 nm, $slit_{ex}$ = 5 nm, $slit_{em}$ = 5 nm, and PMT = 600 V. The spectra were reported after corrections for changes in refractive indices, inner filter effects, and differences in lifetimes of the excited-state species (see Figure S2; Supplemental Experimental Procedures, Correction of Observed Photoluminescence Data). The titration was performed three times in order to obtain the mean and standard deviation of the data.

Preparation of PET_8/1 with Cylindrical Pores Used in Electronic Absorption Measurements

PET films containing 10^8 approximately cylindrical pores per cm^2, which were large enough that they did not rectify ionic current, were fabricated by a procedure that is

similar to a previously described track-etching technique.[57,58,82] Briefly, each template was prepared by bombarding a 12 μm thick PET film with heavy uranium ions whose energy of 11.1 MeV per nucleon generated a single latent track per ion that spanned the thickness of the film (UNILAC, GSI Helmholtz Centre for Heavy Ion Research, Darmstadt, Germany). Cylindrical pores were then produced by an alkaline chemical etching procedure. For better etching results, the films were first irradiated with longwave ultraviolet light on both sides and were then serially rinsed with isopropanol, methanol, and deionized water. The nonporous transparent templates were stirred in aqueous 9 M NaOH at ~80°C for 15 min to create a porous white opaque film.

Successful coupling of **1** was achieved through a two-step procedure using conditions similar to those described by Nakajima and Ikada for 1-ethyl-3-(3-dimethylaminoproypl)carbodiimide (EDC) chemistry in aqueous media.[83] First, the film was rinsed with an unbuffered aqueous solution, titrated with concentrated aqueous HCl to pH 4. Next, the film was placed in an aqueous solution of 0.1 M EDC, 0.1 M *N*-hydroxysuccinimide, and 0.1 M MES buffer (pH 5.0, titrated with aqueous HCl) to activate the surface i.e., convert the carboxylic acids on the PET surface into *o*-acylisourea esters. The films were rinsed with distilled water and then stirred in an aqueous solution of 0.05 M **1**, pH 9 (pre-titrated with aqueous NaOH solution) for ≥24 h.

Electronic Absorption Measurements on PET_8/1 with Cylindrical Pores

An aqueous solution of 0.1 M sodium tetraborate decahydrate, 0.1 M citric acid anhydrous, 0.1 M tris(hydroxymethyl)aminomethane, 0.1 M potassium phosphate monobasic, and 0.1 M potassium chloride was produced. The solution was titrated with concentrated aqueous HCl or 9 M NaOH to the desired pH, as measured using a Fisher Scientific pH/Ion 510. After titrating the solution to the desired pH, the film was stirred for ~1 min in the buffered solution. The film was removed and while dripping wet, pushed flush against the aperture. Ultraviolet–visible electronic absorption spectra were recorded on a Cary 60 UV-Vis Spectrophotometer. To account for the inhomogeneity of the film, each reported spectrum is an average of 10 scans taken at different locations on the film. Lastly, the spectra were baselined with PET_8 modified with ethylenediamine.

Preparation of Single Conical Nanopores Used in Electrochemical Measurements

Conical pores in PET films were fabricated by a previously described track-etching technique.[57,58,82] Briefly, each template was prepared by bombarding a 12 μm thick PET film with heavy uranium ions whose energy of 11.4 MeV per nucleon for PET_0 or 11.1 MeV per nucleon for PET_8 generated a single latent track per ion that spanned the thickness of the film (UNILAC, GSI Helmholtz Centre for Heavy Ion Research, Darmstadt, Germany). Conical nanopore(s) were then produced by an alkaline chemical etching procedure. For better etching results, the films were first irradiated with longwave ultraviolet light on both sides and were then serially rinsed with isopropanol, methanol, and deionized water. The film was then placed in a clean two-chamber cell for subsequent etching: aqueous 9 M NaOH was placed on one side of the film to etch the latent track, while an aqueous stopping medium containing 1 M formic acid and 1 M KCl was placed on the other side of the film to halt the reaction. A platinum (Pt) electrode was placed on each side of the membrane and a 1 V bias was applied to the anode, which was immersed in the aqueous 9 M NaOH solution. An increase in current, indicating a decrease in the resistance across the film, signified pore breakthrough and completed synthesis of a conical nanopore.

The reaction for PET_0 was usually halted when a current of ~200 pA was observed. The resulting nanopore had a large base opening with diameter *A*, which was approximated based on the bulk etch rate for the described etching scenario of 2.13 nm/min. The diameter of the small tip opening, *a*, was approximated by the following equation:

$$R = \frac{4L}{\pi g A a}, \qquad \text{(Equation 5)}$$

where *R* is the resistance of a nanopore, *L* is the length of the pore, and *g* is the specific conductivity of the electrolyte, which was 10 S/m for an aqueous 1 M KCl solution. *R* was determined by calculating the slope of the linear current–potential data between −0.1 V and +0.1 V to obtain the electrical conductance and then reciprocating it.

A PET_0 film was then placed in a two-chamber cell that was subsequently rinsed with a pH 4.0, 100 mM KCl aqueous electrolyte. An aqueous solution of 0.1 M EDC, 0.1 M *N*-hydroxysuccinimide, and 0.01 M MES buffer was titrated to pH 5.0 with dilute aqueous HCl. The EDC solution was placed on both sides of the film and allowed to react for 1 h. Without disassembling the cell, the EDC solution was then removed and electrochemical cell chambers were rinsed twice with deionized water. In a separate beaker, an aqueous 0.05 M **1** solution was titrated to pH 9.0 and placed on both sides of the film for ≥ 24 h. Without disassembling the cell, the solution was removed and the film was rinsed five times with deionized water. The membrane was stored in the cell using an aqueous pH 7.0 electrolyte containing 100 mM KCl and 1 mM tris(hydroxymethyl)aminomethane.

Electrochemical Characterization on PET_0/1 and PET_8/1

Experiments were carried out using a VSP-300 potentiostat (Bio-Logic Science) equipped with low-current cables and a Faraday cage (Bio-Logic Science). The PET_n/**1** was placed in a two-chamber cell and a four-electrode setup was utilized. Two Pt wires served as the working and counter electrodes, while two standard calomel electrodes (SCEs) (KCl saturated) served as the reference electrodes. One of each was placed in chambers on either side of the membrane.

An aqueous 0.1 M KCl stock solution was purged via stirring and the vigorous bubbling of argon. The pH was continuously measured via a Fisher Scientific pH/Ion 510 probe that was immersed in the solution. The stock solution was purged for 20 min before performing the initial cyclic voltammetric titration experiment. The assembled two-chamber cell was rinsed with deionized water five times and then carefully rinsed with purged electrolyte solution five times. Cyclic voltammogram were recorded using the following parameters: a scan rate of 50 mV/s, scan range of 4 V to −4 V versus reference, the scan started and ended at 0 V versus reference, the scan cycle was repeated three times, current was measured over the last 50% of the step duration, recorded current was averaged over 10 voltage steps, the voltage resolution was set to 200 μV, and the current resolution range was set to 10 nA. The electrolyte solution in the cell was not purged during the measurement to prevent interference from bubbles. However, the stock solution was continuously purged during the cyclic voltammogram measurements. Titrations employed aqueous solutions of either HCl or KOH. Salt buildup was attenuated by titrating one purged stock solution from pH ~6 to ~1 with only HCl and titrating another purged stock solution from pH ~6 to ~11 with only KOH. Measurements were performed from pH ~6 to ~1 and then from pH ~6 to ~11.

Determining Binding Coverage of Photoacid in Nanopores

As described above, conical pores in a PET_0 film and PET_8 film were prepared, and the two films were completely modified with **1** to form PET_0/**1** and PET_8/**1**. Separately, **1** was hydrolyzed from both modified films using 5 mL of aqueous 1 M NaOH. Electronic absorption spectra of both samples were recorded on a Cary 60 UV-Vis Spectrophotometer. The binding surface coverage of **1** inside a single nanopore was calculated using Equation S5.

Synthesis and Electronic Absorption Measurements on Trimethyl 4,4′,4″-(((((8-Hydroxypyrene-1,3,6-trisulfonyl)tris(azanediyl))tris(ethane-2,1-diyl))tris(azanediyl))tris(carbonyl))tribenzoate (2)

Methylterephthalate (0.006 g, 3 mmol), EDC (0.008 g, 4 mmol), *N*-hydroxysuccinimide (0.006 g, 5 mmol), and MES buffer (0.005 g, 3 mmol) were added to a mixture of 5 mL of water and 5 mL of methanol. The reaction was stirred at room temperature for 1.5 h. Then, **1** (0.006 g, 0.6 mmol) was added and stirred at room temperature for 0.5 h. The reaction vessel was heated to 60°C and stirred for 4 days. The solution was diluted with deionized water so that major absorption peaks were ~0.3 units. Electronic absorption spectra were recorded on a Cary 60 UV-Vis Spectrophotometer and baselined with deionized water. The cocktail containing **2** was titrated using concentrated aqueous HCl and 9 M NaOH to minimize changes to the concentration of **2**.

Preparation of PET_8/1 with Conical Pores Used in Fluorescence Microscopy Measurements

PET_8 was prepared by the track-etching technique described earlier with the exception that the etchant process was usually halted when a current of ~1 μA was observed instead of ~200 pA. Even though PET_8 contained a factor of $\sim 10^8$ times more heavy-ion irradiated regions, stopping the etchant process at this small of a current value ensured optimal rectification behavior.

The outward-facing surface of PET_8 on the side with the small nanopore tip opening—not in the conical nanopores—was modified with non-fluorescent taurine (T) molecules followed by **1** such that **1** was located primarily inside the tips of the nanopores (PET_8/T+**1**). PET_8 was placed in a two-chamber cell and the cell was rinsed with an aqueous pH 4.0 electrolyte containing 100 mM KCl. Deionized water was placed on the large-pore side of the film. An aqueous solution of 0.1 M EDC, 0.1 M *N*-hydroxysuccinimide, and 0.01 M MES buffer was titrated to pH 5.0 with dilute aqueous HCl. The EDC solution was placed at the tip side of the film and allowed to react for 0.5 min. Without disassembling the cell, the EDC solution was then removed and electrochemical cell chambers were rinsed twice with deionized water. In a separate beaker, an aqueous 0.05 M T solution was titrated to pH 9.0 and placed on both sides of the film for ≥4 h. The cell was rinsed with a pH 4.0, 100 mM KCl aqueous electrolyte. Deionized water was placed on the base side of the film. An aqueous solution of 0.1 M EDC, 0.1 M *N*-hydroxysuccinimide, and 0.01 M MES buffer was titrated to pH 5.0 with dilute aqueous HCl. The EDC solution was placed at the small tip side of the film and allowed to react for 20 min. Without disassembling the cell, the EDC solution was then removed and electrochemical cell chambers were rinsed twice with deionized water. In a separate beaker, an aqueous 0.05 M **1** solution was titrated to pH 9.0 and placed on both sides of the film for ≥24 h. Without disassembling the cell, the solution was removed, and the film was rinsed with deionized water five times. The membrane was stored in the cell and wetted with an aqueous pH 4.0 electrolyte containing 100 mM KCl.

Two-Photon Fluorescence Microscope Setup for Spectral Imaging

A custom-built two-photon-excitation microscope based on an Olympus FLUOVIEW FV1000 (Olympus Corporation, Tokyo, Japan) was used for all fluorescence microscopy experiments. The microscope was equipped with an Olympus UPlanApo 60× water-immersion objective (numerical aperture = 1.2). A mode-locked 80 MHz Ti:Sapphire Chameleon Ultra laser (Coherent, Santa Clara, CA) tunable in the range from 690 nm to 1,040 nm was used for multiphoton excitation. The laser fluence was controlled by an acoustic optical modulator driven by SimFCS (LFD, UCI). A grating-based spectrograph (Andor Shamrock SR-303i) with a 512 channel ultrafast EMCCD (Andor iXon Ultra) was used to collect a spectrum from every pixel with a grating dispersion of 50 lines per meter and a blaze wavelength of 600 nm. In order to ensure spectral acquisition was synced to the frame clock and sampled to the pixel clock, the Olympus FV1000 galvanometer scanning mirrors were driven externally by SimFCS (LFD, UCI) using a data acquisition controller board (IOTECH DAQboard 3001). The spectral images of 256×256 pixels were collected with a pixel dwell time of 32 microseconds. The spectra are corrected with a spectral response curve of the system calibrated using a tungsten lamp, by a technique reported by Chen et al.[84] The multiphoton imaging measurements were carried out with an open pinhole, and the luminescent photons from the microscope were delivered to the spectrograph using a 200 μm multimode optical fiber.

Data Processing of Spectral Images from Two-Photon Fluorescence Microscopy

All data were obtained and analyzed using SimFCS software (Laboratory for Fluorescence Dynamics, UCI, http://www.lfd.uci.edu/globals/, Irvine, CA).

Sample Preparation for Two-Photon Fluorescence Microscopy

PET films were cut to <0.5 cm × <0.5 cm rectangles and placed flat on a glass bottom microwell dish (MatTek Corporation) with the small tip side of the nanopores face down. A titrated solution was pipetted on the film, which did not contain buffer or salt, but instead was pre-titrated with concentrated aqueous solutions of either HCl or NaOH. The film was completely immersed and the solution was pipetted back and forth over the film several times as a means to mix the solution into the nanopores. A glass microscope coverslip was cut and pressed on the top of the film. The solution that protruded from the coverslip side was pipetted away. Enough solution was present in between the glass microwell dish and glass coverslip to completely wet the nanopores.

Unmodified PET and PET_8 whose outward-facing surface on the side with the small nanopore tip opening was modified with T molecules via carbodiimide chemistry (PET_8/T) displayed excitation-wavelength-dependent emission (see Table S4). An excitation wavelength of 900 nm was used to excite the single-photon isosbestic point (~450 nm, Figure 1A). Raw emission spectra from PET_8/T+**1** were individually subtracted by scaled emission spectra of PET_8/T.

SUPPLEMENTAL INFORMATION

Supplemental Information can be found online at https://doi.org/10.1016/j.chempr.2019.04.022.

ACKNOWLEDGMENTS

The authors are grateful for financial support from the Department of Chemistry and the School of Physical Sciences at the University of California Irvine, Research

Corporation for Science Advancement under a Cottrell Scholar Award (award #24169) and the Gordon and Betty Moore Foundation under a Moore Inventor Fellowship (GBMF grant #5641) for S.A. The membranes employed in this work were irradiated during the experiment UMAT, at the beam line X0, at the GSI Helmholtzzentrum fuer Schwerionenforschung, Darmstadt, Germany in the frame of FAIR Phase-0. We thank the UCI Laser Spectroscopy Facility (LSF) for use of photoluminescence spectroscopy instrumentation, the NMR Facility for NMR measurements, and the Mass Spectrometry Facility for mass spectrometry measurements. We also thank Maria Eugenia Toimil-Molares for supplying the heavy-ion irradiated PET films and discussing sample preparation, Zuzanna Siwy and Steven Buchsbaum for training and guidance in nanopore etching and functionalization, Enrico Gratton for use of the Laboratory of Fluorescence Dynamics (LFD) grant number NIH P41-GM103540, Jonathan Lam for general synthetic advice, and Alan Heyduk for use of his laboratory space and his group members for support and guidance.

AUTHOR CONTRIBUTIONS

S.A. proposed the research. C.D.S. synthesized molecules, prepared samples, performed measurements, and analyzed the data with advice from S.A., J.V.C., and M.D. S.A. and C.D.S. prepared the manuscript.

DECLARATION OF INTERESTS

S.A. and C.D.S. are co-inventors on the following pending patent applications that are relevant to this manuscript: US20180065095A1 and WO2018049061A1. S.A. receives sponsored research funding support by Nissan Chemical Corporation for work related to that reported in this manuscript.

Received: September 17, 2018
Revised: January 8, 2019
Accepted: April 24, 2019
Published: June 6, 2019

REFERENCES AND NOTES

1. Memming, R. (2015). Semiconductor Electrochemistry, Second Edition (Wiley-VCH).
2. Yasui, M., Hazama, A., Kwon, T.H., Nielsen, S., Guggino, W.B., and Agre, P. (1999). Rapid gating and anion permeability of an intracellular aquaporin. Nature *402*, 184–187.
3. Jiang, Y., Lee, A., Chen, J., Ruta, V., Cadene, M., Chait, B.T., and MacKinnon, R. (2003). X-ray structure of a voltage-dependent K^+ channel. Nature *423*, 33–41.
4. Bean, B.P. (2007). The action potential in mammalian central neurons. Nat. Rev. Neurosci *8*, 451–465.
5. Andérasson, L.E., and Vänngård, T. (1998). Photosystems I and II. Annu. Rev. Plant Physiol. Plant Mol. Biol. *39*, 379–411.
6. Furshpan, E.J., and Potter, D.D. (1959). Transmission at the giant motor synapses of the crayfish. J. Physiol *145*, 289–325.
7. Phelan, P., Goulding, L.A., Tam, J.L.Y., Allen, M.J., Dawber, R.J., Davies, J.A., and Bacon, J.P. (2008). Molecular mechanism of rectification at identified electrical synapses in the Drosophila giant fiber system. Curr. Biol. *18*, 1955–1960.
8. Glaaser, I.W., and Slesinger, P.A. (2017). Dual activation of neuronal G protein-gated inwardly rectifying potassium (GIRK) channels by cholesterol and alcohol. Sci. Rep *7*, 4592.
9. Lee, I., Lee, J.W., and Greenbaum, E. (1997). Biomolecular electronics: vectorial arrays of photosynthetic reaction centers. Phys. Rev. Lett. *79*, 3294–3297.
10. Simons, R., and Khanarian, G. (1976). Water dissociation in bipolar membranes - experiment and theory. J. Membr. Biol. *38*, 11–30.
11. Bassignana, I.C., and Reiss, H. (1983). Ion transport and water dissociation in bipolar ion exchange membranes. J. Memb. Sci. *15*, 27–41.
12. Ramírez, P., Rapp, H.-J., Mafé, S., and Bauer, B. (1994). Bipolar membranes under forward and reverse bias conditions. Theory vs. experiment. J. Electroanal. Chem. *375*, 101–108.
13. Mafé, S., and Ramírez, P. (1997). Electrochemical characterization of polymer ion-exchange bipolar membranes. Acta Polym *48*, 234–250.
14. Wilhelm, F.G., van der Vegt, N.F.A., Strathmann, H., and Wessling, M. (2002). Comparison of bipolar membranes by means of chronopotentiometry. J. Memb. Sci. *199*, 177–190.
15. Chen, P., Mitsui, T., Farmer, D.B., Golovchenko, J., Gordon, R.G., and Branton, D. (2004). Atomic layer deposition to fine-tune the surface properties and diameters of fabricated nanopores. Nano Lett. *4*, 1333–1337.
16. Li, J., Stein, D., McMullan, C., Branton, D., Aziz, M.J., and Golovchenko, J.A. (2001). Ion-beam sculpting at nanometre length scales. Nature *412*, 166–169.
17. Kong, Y., Fan, X., Zhang, M., Hou, X., Liu, Z., Zhai, J., and Jiang, L. (2013). Nanofluidic diode based on branched alumina nanochannels with tunable ionic rectification. ACS Appl. Mater. Interfaces *5*, 7931–7936.
18. Siwy, Z., Dobrev, D., Neumann, R., Trautmann, C., and Voss, K. (2003). Electro-responsive asymmetric nanopores in polyimide with stable ion-current signal. Appl. Phys. A *76*, 781–785.
19. Siwy, Z., Apel, P., Baur, D., Dobrev, D.D., Korchev, Y.E., Neumann, R., Spohr, R., Trautmann, C., and Voss, K.O. (2003).

Preparation of synthetic nanopores with transport properties analogous to biological channels. Surf. Sci. *532–535*, 1061–1066.

20. Chtanko, N., Molares, M.E.T., Cornelius, T., Dobrev, D., and Neumann, R. (2004). Etched single-ion-track templates for single nanowire synthesis. J. Phys. Chem. B *108*, 9950–9954.

21. Kalman, E., Healy, K., and Siwy, Z.S. (2007). Tuning ion current rectification in asymmetric nanopores by signal mixing. Europhys. Lett. *78*, 28002.

22. Zhang, B., Zhang, Y., and White, H.S. (2004). The nanopore electrode. Anal. Chem. *76*, 6229–6238.

23. Siwy, Z., Heins, E., Harrell, C.C., Kohli, P., and Martin, C.R. (2004). Conical-nanotube ion-current rectifiers: the role of surface charge. J. Am. Chem. Soc. *126*, 10850–10851.

24. Siwy, Z., Gu, Y., Spohr, H.A., Baur, D., Wolf-Reber, A., Spohr, R., Apel, P., and Korchev, Y.E. (2002). Rectification and voltage gating of ion currents in a nanofabricated pore. Europhys. Lett. *60*, 349–355.

25. Siwy, Z.S. (2006). Ion-current rectification in nanopores and nanotubes with broken symmetry. Adv. Funct. Mater *16*, 735–746.

26. Nguyen, G., Vlassiouk, I., and Siwy, Z.S. (2010). Comparison of bipolar and unipolar ionic diodes. Nanotechnology *21*, 265301.

27. Wei, C., Bard, A.J., and Feldberg, S.W. (1997). Current rectification at quartz nanopipet electrodes. Anal. Chem. *69*, 4627–4633.

28. Bruckbauer, A., Ying, L., Rothery, A.M., Zhou, D., Shevchuk, A.I., Abell, C., Korchev, Y.E., and Klenerman, D. (2002). Writing with DNA and protein using a nanopipet for controlled delivery. J. Am. Chem. Soc. *124*, 8810–8811.

29. Piper, J.D., Clarke, R.W., Korchev, Y.E., Ying, L., and Klenerman, D. (2006). A renewable nanosensor based on a glass nanopipette. J. Am. Chem. Soc. *128*, 16462–16463.

30. Umehara, S., Pourmand, N., Webb, C.D., Davis, R.W., Yasuda, K., and Karhanek, M. (2006). Current rectification with poly-L-lysine-coated quartz nanopipettes. Nano Lett. *6*, 2486–2492.

31. McKelvey, K., German, S.R., Zhang, Y., White, H.S., and Edwards, M.A. (2017). Nanopipettes as a tool for single nanoparticle electrochemistry. Curr. Opin. Electrochem *6*, 4–9.

32. Guerrette, J.P., and Zhang, B. (2010). Scan-rate-dependent current rectification of cone-shaped silica nanopores in quartz nanopipettes. J. Am. Chem. Soc. *132*, 17088–17091.

33. Sun, K., and Mauzerall, D. (1996). A simple light-driven transmembrane proton pump. Proc. Natl. Acad. Sci. USA *93*, 10758–10762.

34. Steinberg-Yfrach, G., Liddell, P.A., Hung, S.-C., Moore, A.L., Gust, D., and Moore, T.A. (1997). Conversion of light energy to proton potential in liposomes by artificial photosynthetic reaction centres. Nature *385*, 239–241.

35. Bhosale, S., Sisson, A.L., Talukdar, P., Fürstenberg, A., Banerji, N., Vauthey, E., Bollot, G., Mareda, J., Röger, C., Würthner, F., et al. (2006). Photoproduction of proton gradients with π-stacked fluorophore scaffolds in lipid bilayers. Science *313*, 84–86.

36. Xie, X., Crespo, G.A., Mistlberger, G., and Bakker, E. (2014). Photocurrent generation based on a light-driven proton pump in an artificial liquid membrane. Nat. Chem. *6*, 202–207.

37. White, W., Sanborn, C.D., Reiter, R.S., Fabian, D.M., and Ardo, S. (2017). Observation of photovoltaic action from photoacid-modified nafion due to light-driven ion transport. J. Am. Chem. Soc. *139*, 11726–11733.

38. Soroka, H.P., Simkovitch, R., Kosloff, A., Shomer, S., Pevzner, A., Tzang, O., Tirosh, R., Patolsky, F., and Huppert, D. (2013). Excited-state proton transfer and proton diffusion near hydrophilic surfaces. J. Phys. Chem. C *117*, 25786–25797.

39. White, W., Sanborn, C.D., Fabian, D.M., and Ardo, S. (2018). Conversion of visible light into ionic power using photoacid-dye-sensitized bipolar ion-exchange membranes. Joule *2*, 94–109.

40. Wen, L., Hou, X., Tian, Y., Nie, F.Q., Song, Y., Zhai, J., and Jiang, L. (2010). Bioinspired smart gating of nanochannels toward photoelectric-conversion systems. Adv. Mater *22*, 1021–1024.

41. Xiao, K., Xie, G., Li, P., Liu, Q., Hou, G., Zhang, Z., Ma, J., Tian, Y., Wen, L., and Jiang, L. (2014). A biomimetic multi-stimuli-response ionic gate using a hydroxypyrene derivation-functionalized asymmetric single nanochannel. Adv. Mater *26*, 6560–6565.

42. Tolbert, L.M., and Solntsev, K.M. (2002). Excited-state proton transfer: from constrained systems to "super" photoacids to superfast proton transfer. Acc. Chem. Res. *35*, 19–27.

43. Würfel, P. (2005). Physics of Solar Cells, First Edition (Wiley-VCH).

44. Gutman, M., and Huppert, D. (1979). Rapid pH and deltamuH+ jump by short laser pulse. J. Biochem. Biophys. Methods *1*, 9–19.

45. Gutman, M., Huppert, D., and Pines, E. (1981). The pH jump: a rapid modulation of pH of aqueous solutions by a laser pulse. J. Am. Chem. Soc. *103*, 3709–3713.

46. Mauritz, K.A., and Moore, R.B. (2004). State of understanding of nafion. Chem. Rev. *104*, 4535–4585.

47. Gaieck, W., and Ardo, S. (2014). Challenges and opportunities for ion-exchange membranes in solar fuels devices. Rev. Adv. Sci. Eng *3*, 277–287.

48. Kusoglu, A., and Weber, A.Z. (2017). New insights into perfluorinated sulfonic-acid ionomers. Chem. Rev. *117*, 987–1104.

49. Onufriev, A., Case, D.A., and Ullmann, G.M. (2001). A novel view of pH titration in biomolecules. Biochemistry *40*, 3413–3419.

50. Finkler, B., Spies, C., Vester, M., Walte, F., Omlor, K., Riemann, I., Zimmer, M., Stracke, F., Gerhards, M., and Jung, G. (2014). Highly photostable "super"-photoacids for ultrasensitive fluorescence spectroscopy. Photochem. Photobiol. Sci. *13*, 548–562.

51. Das, I., Panja, S., and Halder, M. (2016). Modulation and salt-induced reverse modulation of the excited-state proton-transfer process of lysozymized pyranine: the contrasting scenario of the ground-state acid-base equilibrium of the photoacid. J. Phys. Chem. B *120*, 7076–7087.

52. Hercules, D.M., and Rogers, L.B. (1959). Luminescence spectra of naphthols and naphthalenediols low temperature phenomena. J. Phys. Chem. *64*, 397–400.

53. Wehry, E.L., and Rogers, L.B. (1965). Variation of excited-state pKa values with method of measurement. Spectrochim. Acta *21*, 1976–1978.

54. Ireland, J.F., and Wyatt, P.A.H. (1976). Acid-base properties of electronically excited states of organic molecules. Adv. Phys. Org. Chem. *12*, 131–221.

55. O'Donnell, R.M., Sampaio, R.N., Li, G., Johansson, P.G., Ward, C.L., and Meyer, G.J. (2016). Photoacidic and photobasic behavior of transition metal compounds with carboxylic acid Group(s). J. Am. Chem. Soc. *138*, 3891–3903.

56. Apel, P. (2001). Track etching technique in membrane technology. Radiat. Meas. *34*, 559–566.

57. Apel, P.Y., Korchev, Y.E., Siwy, Z., Spohr, R., and Yoshida, M. (2001). Diode-like single-ion track membrane prepared by electro-stopping. Nucl. Instrum. Methods Phys. Res. B *184*, 337–346.

58. Vlassiouk, I., and Siwy, Z.S. (2007). Nanofluidic diode. Nano Lett. *7*, 552–556.

59. Siwy, Z., and Fuliński, A. (2004). A nanodevice for rectification and pumping ions. Am. J. Phys. *72*, 567–574.

60. Constantin, D., and Siwy, Z.S. (2007). Poisson-Nernst-Planck model of ion current rectification through a nanofluidic diode. Phys. Rev. E Stat. Nonlin. Soft Matter Phys. *76*, 041202.

61. Xue, J.M., Zou, X.Q., Xie, Y.B., and Wang, Y.G. (2009). Molecular dynamics simulations on the ionic current through charged nanopores. J. Phys. D: Appl. Phys. *42*, 105308.

62. Kovarik, M.L., Zhou, K., and Jacobson, S.C. (2009). Effect of conical nanopore diameter on ion current rectification. J. Phys. Chem. B *113*, 15960–15966.

63. Siwy, Z.S., and Howorka, S. (2010). Engineered voltage-responsive nanopores. Chem. Soc. Rev. *39*, 1115–1132.

64. He, Y., Gillespie, D., Boda, D., Vlassiouk, I., Eisenberg, R.S., and Siwy, Z.S. (2009). Tuning transport properties of nanofluidic devices with local charge inversion. J. Am. Chem. Soc. *131*, 5194–5202.

65. Ali, M., Schiedt, B., Healy, K., Neumann, R., and Ensinger, W. (2008). Modifying the surface charge of single track-etched conical nanopores in polyimide. Nanotechnology *19*, 085713.

66. Ali, M., Ramirez, P., Mafé, S., Neumann, R., and Ensinger, W. (2009). A pH-tunable nanofluidic diode with a broad range of rectifying properties. ACS Nano *3*, 603–608.

67. Yameen, B., Ali, M., Neumann, R., Ensinger, W., Knoll, W., and Azzaroni, O. (2009). Synthetic proton-gated ion channels via single solid-state nanochannels modified with responsive polymer brushes. Nano Lett. *9*, 2788–2793.

68. Yameen, B., Ali, M., Neumann, R., Ensinger, W., Knoll, W., and Azzaroni, O. (2010). Proton-regulated rectified ionic transport through solid-state conical nanopores modified with phosphate-bearing polymer brushes. Chem. Commun. (Camb.) *46*, 1908–1910.

69. Gilles, F.M., Tagliazucchi, M., Azzaroni, O., and Szleifer, I. (2016). Ionic conductance of polyelectrolyte-modified nanochannels: nanoconfinement effects on the coupled protonation equilibria of polyprotic brushes. J. Phys. Chem. C *120*, 4789–4798.

70. Tagliazucchi, M., Azzaroni, O., and Szleifer, I. (2010). Responsive polymers end-tethered in solid-state nanochannels: when nanoconfinement really matters. J. Am. Chem. Soc. *132*, 12404–12411.

71. Siwy, Z., Apel, P., Dobrev, D., Neumann, R., Spohr, R., Trautmann, C., and Voss, K. (2003). Ion transport through asymmetric nanopores prepared by ion track etching. Nucl. Instrum. Methods Phys. Res. B *208*, 143–148.

72. Yameen, B., Ali, M., Neumann, R., Ensinger, W., Knoll, W., and Azzaroni, O. (2009). Single conical nanopores displaying pH-tunable rectifying characteristics. Manipulating ionic transport with zwitterionic polymer brushes. J. Am. Chem. Soc. *131*, 2070–2071.

73. Ali, M., Yameen, B., Cervera, J., Ramírez, P., Neumann, R., Ensinger, W., Knoll, W., and Azzaroni, O. (2010). Layer-by-layer assembly of polyelectrolytes into ionic current rectifying solid-state nanopores: insights from theory and experiment. J. Am. Chem. Soc. *132*, 8338–8348.

74. Cervera, J., Schiedt, B., Neumann, R., Mafé, S., and Ramírez, P. (2006). Ionic conduction, rectification, and selectivity in single conical nanopores. J. Chem. Phys. *124*, 104706.

75. Spry, D.B., Goun, A., Glusac, K., Moilanen, D.E., and Fayer, M.D. (2007). Proton transport and the water environment in nafion fuel cell membranes and AOT reverse micelles. J. Am. Chem. Soc. *129*, 8122–8130.

76. Spry, D.B., and Fayer, M.D. (2009). Proton transfer and proton concentrations in protonated nafion fuel cell membranes. J. Phys. Chem. B *113*, 10210–10221.

77. Piletic, I.R., Tan, H.S., and Fayer, M.D. (2005). Dynamics of nanoscopic water: vibrational echo and infrared pump-probe studies of reverse micelles. J. Phys. Chem. B *109*, 21273–21284.

78. Tan, H.S., Piletic, I.R., and Fayer, M.D. (2005). Orientational dynamics of water confined on a nanometer length scale in reverse micelles. J. Chem. Phys. *122*, 174501.

79. Tan, H.S., Piletic, I.R., Riter, R.E., Levinger, N.E., and Fayer, M.D. (2005). Dynamics of water confined on a nanometer length scale in reverse micelles: ultrafast infrared vibrational echo spectroscopy. Phys. Rev. Lett. *94*, 057405.

80. Zhang, Z., Kong, X.Y., Xie, G., Li, P., Xiao, K., Wen, L., and Jiang, L. (2016). "Uphill" cation transport: a bioinspired photodriven ion pump. Sci. Adv *2*, e1600689.

81. Zhang, Z., Wen, L., and Jiang, L. (2018). Bioinspired smart asymmetric nanochannel membranes. Chem. Soc. Rev. *47*, 322–356.

82. Spohr, R. (1983). Methods for producing nuclear traces or microholes originating from nuclear traces of an individual ion, United States Patent 4369370.

83. Nakajima, N., and Ikada, Y. (1995). Mechanism of amide formation by carbodiimide for bioconjugation in aqueous media. Bioconjug. Chem. *6*, 123–130.

84. Chen, H., Gratton, E., and Digman, M.A. (2015). Spectral properties and dynamics of gold nanorods revealed by EMCCD-based spectral phasor method. Microsc. Res. Tech *78*, 283–293.